

Effect of aggregation on thermally activated delayed fluorescence and ultralong organic phosphorescence: QM/MM study

Qun Zhang(张群), Xiaofei Wang(王晓菲), Zhimin Wu(吴智敏), Xiaofang Li(李小芳), Kai Zhang(张凯), Yuzhi Song(宋玉志), Jianzhong Fan(范建忠), Chuan-Kui Wang(王传奎), and Lili Lin(蔺丽丽)
Citation: Chin. Phys. B, 2023, 32 (**10**): 103301. DOI: 10.1088/1674-1056/acb75d
Journal homepage: http://cpb.iphy.ac.cn; http://iopscience.iop.org/cpb

What follows is a list of articles you may be interested in

Theoretical verification of intermolecular hydrogen bond induced thermally activated delayed fluorescence in SOBF-Ome

Mu-Zhen Li(李慕臻), Fei-Yan Li(李飞雁), Qun Zhang(张群), Kai Zhang(张凯), Yu-Zhi Song(宋玉志), Jian-Zhong Fan(范建忠), Chuan-Kui Wang(王传奎), and Li-Li Lin(蔺丽丽)
Chin. Phys. B, 2021, 30 (**12**): 123302. DOI: 10.1088/1674-1056/ac1b91

Effects of temperature and pressure on OH laser-induced fluorescence exciting A-X (1,0) transition at high pressures

Xiaobo Tu(涂晓波), Linsen Wang(王林森), Xinhua Qi(齐新华), Bo Yan(闫博), Jinhe Mu(母金河), Shuang Chen(陈爽)
Chin. Phys. B, 2020, 29 (**9**): 093301. DOI: 10.1088/1674-1056/aba5ff

Energy transfer, luminescence properties, and thermal stability of color tunable barium pyrophosphate phosphors

Meng-Jiao Xu(徐梦姣), Su-Xia Li(李素霞), Chen-Chen Ji(季辰辰), Wan-Xia Luo(雒晚霞), Lu-Xiang Wang(王鲁香)
Chin. Phys. B, 2020, 29 (**6**): 063301. DOI: 10.1088/1674-1056/ab821a

Exploring photocurrent output from donor/acceptor bulk-heterojunctions by monitoring exciton quenching

Wang Xin-Ping (王新平), He Zhi-Qun (何志群), Liang Chun-Jun (梁春军), Qiu Hai-An (邱海安), Jing Xi-Ping (荆西平)
Chin. Phys. B, 2015, 24 (**6**): 063301. DOI: 10.1088/1674-1056/24/6/063301

Fine-tuning the thicknesses of organic layers to realize high-efficiency and long-lifetime blue organic light-emitting diodes

Yu Jian-Ning (于建宁), Zhang Min-Yan (张民艳), Li Chong (李崇), Shang Yu-Zhu (尚玉柱), Lü Yan-Fang (吕燕芳), Wei Bin (魏斌), Huang Wei (黄维)
Chin. Phys. B, 2012, 21 (**8**): 083303. DOI: 10.1088/1674-1056/21/8/083303

Effect of aggregation on thermally activated delayed fluorescence and ultralong organic phosphorescence: QM/MM study

Qun Zhang(张群), Xiaofei Wang(王晓菲), Zhimin Wu(吴智敏), Xiaofang Li(李小芳), Kai Zhang(张凯), Yuzhi Song(宋玉志), Jianzhong Fan(范建忠), Chuan-Kui Wang(王传奎)[†], and Lili Lin(蔺丽丽)[‡]

Shandong Key Laboratory of Medical Physics and Image Processing & Shandong Provincial Engineering and Technical Center of Light Manipulations, School of Physics and Electronics, Shandong Normal University, Jinan 250358, *China*

(Received 1 October 2022; revised manuscript received 22 January 2023; accepted manuscript online 31 January 2023)

Aggregation-induced thermally activated delayed fluorescence (TADF) phenomena have attracted extensive attention recently. In this paper, several theoretical models including monomer, dimer, and complex are used for the explanation of the luminescent properties of (*R*)-5-(9H-carbazol-9-yl)-2-(1,2,3,4-tetrahydronaphthalen-1-yl)isoindoline-1,3-dione ((*R*)-ImNCz), which was recently reported [*Chemical Engineering Journal* **418** 129167 (2021)]. The polarizable continuum model (PCM) and the combined quantum mechanics and molecular mechanics (QM/MM) method are adopted in simulation of the property of the molecule in the gas phase, solvated in acetonitrile and in aggregation states. It is found that large spin–orbit coupling (SOC) constants and a smaller energy gap between the first singlet excited state and the first triplet excited state (ΔE_{st}) in prism-like single crystals (SC_p-form) are responsible for the TADF of (*R*)-lmNCz, while no TADF is found in block-like single crystals (SC_b-form) with a larger ΔE_{st}. The multiple ultralong phosphorescence (UOP) peaks in the spectrum are of complex origins, and they are related not only to ImNCz but also to a minor amount of impurities (ImNBd) in the crystal prepared in the laboratory. The dimer has similar phosphorescence emission wavelengths to the (*R*)-lmNCz-SC_p monomers. The complex composed of (*R*)-lmNCz and (*R*)-lmNBd contributes to the phosphorescent emission peak at about 600 nm, and the phosphorescent emission peak at about 650 nm is generated by (*R*)-lmNBd. This indicates that the impurity could also contribute to emission in molecular crystals. The present calculations clarify the relationship between the molecular aggregation and the light-emitting properties of the TADF emitters and will therefore be helpful for the design of potentially more useful TADF emitters.

Keywords: organic light-emitting diodes, thermally activated delayed fluorescence, ultralong organic phosphorescence, aggregation mode

PACS: 33.50.–j, 33.50.Dq, 33.50.Hv **DOI:** 10.1088/1674-1056/acb75d

1. Introduction

In the past few years, extensive attention has been paid to organic thermally activated delayed fluorescence (TADF) emitters due to their unique photophysical properties.[1–4] Since Pope and others first reported organic electroluminescent materials in 1963,[5] organic electroluminescent materials have gradually entered the public's field of vision, especially in the fields of solid-state lighting, display panels, organic light-emitting diode (OLED) TV, digital cameras, and so on.[6–8] TADF materials are generally supposed to be the third generation of organic light-emitting materials after traditional fluorescent materials and traditional phosphorescent materials, with their internal quantum efficiency (IQE) reaching 100%.[9–16] For TADF materials, the excitons in the triplet state cross to the singlet state through reverse intersystem crossing (RISC) on thermal activation, and thereafter emit delayed fluorescence from the singlet state to the ground state. The implementation of the TADF process requires a small energy gap between the first singlet excited state and the first triplet excited state (ΔE_{st}), which can be realized by a small overlap between the highest occupied molecular orbital (HOMO) and the lowest unoccupied molecular orbital (LUMO). The general method to obtain TADF is to use a molecular design strategy combining donor and acceptor groups.[17–22] Of course, molecular aggregation behavior can also induce and regulate the TADF process. In recent years, there have been preliminary studies on the law of accumulation modes in TADF behavior. It is found that J-aggregation can reduce ΔE_{st}, which promotes the RISC process and TADF process, in general. H-aggregation promotes the intersystem crossing (ISC) process and weakens TADF, but promotes the RTP process.[23] In 2019, Thilagar *et al.* reported that a molecule crystallized in two different crystal forms (1a and 1b).[24] Polymorph 1b with J-aggregation has brighter TADF phenomenon than polymorph 1a with a random arrangement. In the same year, Yang *et al.* reported two DMAC-CNQ and FDMAC-CNQ molecules with multi-functional emission, and realized TADF, AIE and MCL by regulating their aggregation mode.[25] In 2021, Yang *et al.* found the regulation of aggregation state on TADF in TRZ-c-BPXZ and TRZ-a-BPXZ molecules.[26] In the same year, Fu *et al.* found J-aggregation state regulation on TADF in the (*E*)-5-(ethoxycarbonyl)-2,2-

[†]Corresponding author. E-mail: ckwang@sdnu.edu.cn
[‡]Corresponding author. E-mail: linll@sdnu.edu.cn

© 2023 Chinese Physical Society and IOP Publishing Ltd

difluoro-6-methyl-4-(2-[1-methyl-1H-indol-2-yl]vinyl)-2H-1,3,2-dioxaborinin-1-ium-2-uide molecule.[27] However, there are few studies of the aggregation effect on TADF properties theoretically, due to the difficulty in the simulation of aggregation states. In addition, the complicity in aggregation states makes it more difficult to understand the light-emitting properties.

Recently, a pair of chiral TADF molecules (*R*)-5-(9H-carbazol-9-yl)-2-(1,2,3,4-tetrahydronaphthalen-1-yl)isoindoline-1,3-dione [(*R*)-lmNCz] and (*S*)-5-(9H-carbazol-9-yl)-2-(1,2,3,4-tetrahydronaphthalen-1-yl)isoindoline-1,3-dione [(*S*)-lmNCz] (as shown in Figs. 1(a)–(d)) have been reported.[28] The block-like single crystals (SC_b-form) and prism-like single crystals (SC_p-form) of (*R*/*S*)-lmNCz are found to have different luminescent properties. The multiple ultralong phosphorescence (UOP) peaks in the spectrum were of complex origins, and they are related not only to ImNCz but also to a small amount of impurities (ImNBd) in the crystal prepared in the laboratory. There is no TADF phenomenon in the SC_b-form, while TADF phenomenon is found in the SC_p-form. We believe that this is related to their different aggregation methods. The SC_b-form shows face-to-face stacking and the SC_p-form adopts edge stacking. The SC_p crystal has a wide frequency band in the range of 430–520 nm and three peaks in the range of 520–700 nm. In order to verify the generation mechanism of TADF and RTP in SC_p crystals and the absence of TADF in SC_b crystals, the luminescence characteristics of the chiral molecules in the crystalline state are studied by combining quantum mechanics and molecular mechanics (QM/MM) methods. At the same time, the luminescence characteristics of (*R*)-lmNCz, (*S*)-lmNCz, and (*R*)-lmNBd in acetonitrile solution are studied using the polarizable continuum model (PCM). Recently, Li and Zhang *et al.* performed theoretical studies on SOBF-OMe and DBPz-2spAc with PCM and QM/MM methods, and good agreement with experimental results was obtained, which indicates the reliability of this method.[29,30] Nevertheless, these calculation models were limited to only the ONIOM model of single components. In this study, the impurity in the crystal is also considered to explain the emission spectra, which indicates that the impurity could also participate in the emission. The photoluminescence properties of (*R*)-lmNCz, (*S*)-lmNCz, and (*R*)-lmNBd in gas phase are also studied. Both monomers and dimers are selected as research models to explore the origin of TADF. Our existing calculation results demonstrate that the generation of broadband is closely related to the radiation transition of S_1. The three peaks in the range of 520–700 nm (as shown in Fig. 1(e)) should be due to a small amount of (*R*)-lmNBd impurities in the crystals prepared in the laboratory, which agree with experimental guess.[31] Our theoretical simulation results provide a reasonable explanation for the generation mechanism of TADF and RTP, which is helpful to understand the influence of molecular stacking mode on luminescence properties.

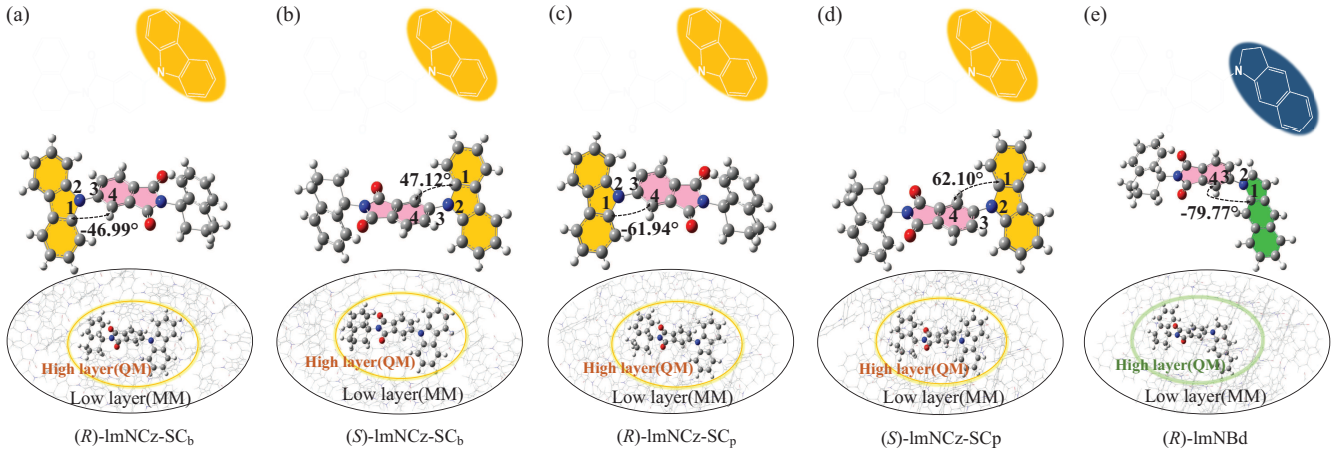


Fig. 1. Molecular structures and ONIOM model of (*R*)-lmNCz-SC_b, (*S*)-lmNCz-SC_b, (*R*)-lmNCz-SC_p, (*S*)-lmNCz-SC_p, and (*R*)-lmNBd. The centered molecule is treated as the high layer and surrounding molecules are regarded as the low layer.

2. Theoretical methods and calculation details

In this work, the luminescence characteristics of (*R*)-lmNCz, (*S*)-lmNCz, and (*R*)-lmNBd in acetonitrile solution are simulated with the PCM method which has turned out to be a trustworthy tool for predicting the influence of solvents on TADF molecules.[32,33] The calculation model is established according to the four crystal structures obtained from the experiment (as shown in Fig. 1).[28] A two-layer ONIOM method is adopted for the molecular crystal simulation.[34–37] The central molecule is chosen as the high layer and measured by the QM method, while the surrounding molecules are selected as the low layer and determined by the MM method. The calculation of the ground state and excited state of the high layer molecule in the center is based on density functional theory (DFT) and time-dependent density functional theory (TD-DFT), respectively.[38] For the surrounding molecules, the universal force field (UFF) which sustains major elements

is applied, which has also been proven reliable.[39,40] In the optimization process, the central molecule is completely released, while other molecules are locked. In our study, the ONIOM model of (*R*)-lmNBd (as shown in Fig. 1(e)) is constructed by replacing a (*R*)-lmNCz molecule in the SC_p crystal of (*R*)-lmNCz, and the replacement (*R*)-lmNBd is set as the central molecule in the ONIOM model. For the sake of researching the interaction between (*R*)-lmNCz molecules and surrounding (*R*)-lmNCz molecules, a dimer is taken as central molecule based on the ONIOM model. In order to study the interaction between the (*R*)-lmNBd molecule and surrounding (*R*)-lmNCz molecules, an (*R*)-lmNBd molecule and an (*R*)-lmNCz molecule are taken as a complex in the ONIOM model. The geometries of the dimer and complex are shown in Fig. S1. The intermolecular interactions of (*R*)-lmNCz, (*S*)-lmNCz, and (*R*)-lmNBd are assessed by the independent gradient model based on Hirshfeld partition (IGMH).[41] QM/MM methods are also used to calculate the photophysical properties of the dimer and the complex. Five functionals (WB97XD, PBE0, M062X, BMK, and B3LYP) are tested on the emission wavelengths together with a 6-31G* basis set (as shown in Table 1).[42–46] Functional fitting results show that the fluorescence wavelengths of (*R*)-lmNCz-SC_b, (*S*)-lmNCz-SC_b, (*R*)-lmNCz-SC_p, and (*S*)-lmNCz-SC_p fit well with the experimental values at the PBE0/6-31G* level. Therefore, all the operations of the following QM parts are performed at the PBE0/6-31 G* level. All these corresponding calculations are implemented in the Gaussian 16 package.[47]

Table 1. Emission wavelengths calculated by different functionals for (*R*)-lmNCz-SC_b, (*S*)-lmNCz-SC_b, (*R*)-lmNCz-SC_p, and (*S*)-lmNCz-SC_p in the solid phase (unit: nm).

	(*R*)-lmNCz-SC_b	(*S*)-lmNCz-SC_b	(*R*)-lmNCz-SC_p	(*S*)-lmNCz-SC_p
Wb97xd	359	342	350	339
Pbe0	497	451	497	465
M062x	376	353	370	354
Bmk	413	382	409	388
B3lyp	544	489	547	508
Exp.	482	482	459	465

Efficient intersystem crossing rates and reverse intersystem crossing rates (K_{ISC}, K_{RISC}) are significant indicators to measure the TADF process and the RTP process. The K_{ISC} between two electronic states with different spin states can be described as[48,49]

$$K_{ISC} = \frac{1}{\hbar^2}\left\langle \Phi_f|H^{SO}|\Phi_i\right\rangle \times \int_{-} \mathrm{d}t\left[\mathrm{e}^{\mathrm{i}\omega_{if}t}Z_i^{-1}\rho_{ISC}(t,T)\right], \quad (1)$$

where Z_i is the partition function and $\rho_{ISC}(t,T)$ is the thermal vibration correlation function. $\left\langle \Phi_f|\hat{H}^{SO}|\Phi_i\right\rangle$ is the spin–orbit coupling (SOC) between two states with different spin multiplicity, which can be calculated by quadratic response function methods in the Dalton Program.[50] K_{RISC} can also be calculated making use of Eq. (1). The ISC and RISC rates are all calculated using molecular materials property prediction package (MOMAP).[51]

In addition, the radiation rate (K_r) is calculated by the Einstein spontaneous emission equation[52]

$$K_r = \frac{f\Delta E_{fi}^2}{1.499\ \mathrm{cm}^{-2}\cdot\mathrm{s}}, \quad (2)$$

where f is oscillator strength and ΔE_{fi} is the vertical emission energy between the first singlet excited state (S_1) and ground state (S_0) (or between the first triplet excited state (T_1) and S_0) in the units of wavenumber (cm^{-1}).

Furthermore, the non-radiative decay rate from S_1 to S_0 (K_{nr}^1) can be deduced based on first-order perturbation theory and Fermi's golden rule (FGR). Through Fourier transform, it can be written as

$$K_{nr} = \sum_{kl}\frac{1}{\hbar^2}R_{kl}\int_{-}\mathrm{d}t\left[\mathrm{e}^{\mathrm{i}\omega_{if}t}Z_i^{-1}\rho_{IC,kl}(t,T)\right], \quad (3)$$

where $\rho_{IC,kl}(t,T) = \mathrm{tr}(\hat{P}_{fk}\,\mathrm{e}^{-\mathrm{i}\tau_f\hat{H}_f}\hat{P}_{fl}\,\mathrm{e}^{-\mathrm{i}\tau_i\hat{H}_i})$ is the thermal vibration correlation function (TVCF). Z_i is the partition function. $R_{kl} = \left\langle \Phi_f|\hat{P}_{fk}|\Phi_i\right\rangle\left\langle \Phi_i|\hat{P}_{fl}|\Phi_f\right\rangle$ is the non-adiabatic electronic coupling.[53]

As for the non-radiative decay rate from T_1 to S_0 (K_{nr}^2), it can be calculated by the following formula:[54]

$$\ln[K_{nr}(T_n\to S_0)] = -\frac{(\Delta E_{ad}-\sum_j\lambda_j)^2}{4\sum_j\lambda_j E_j} + \ln\left(\frac{1}{\hbar}|\langle S_0|\hat{H}^{SO}|T_n\rangle|^2\sqrt{\frac{\pi}{\sum_j\lambda_j\bar{E}_j}}\right). \quad (4)$$

Here, ΔE_{ad} represents the adiabatic excitation energy and λ_j refers to the reorganization energy of the jth vibrational mode. $|\langle S_0|\hat{H}^{SO}|T_n\rangle|$ is the SOC matrix element between S_0 and T_n.

The Huang–Rhys factor and recombination energy are obtained using the DUSHIN software package for normal mode analyses on the obtained geometric structure and electronic structure information. The Huang–Rhys factor and reorganization energy formula can be written as

$$HR_k = \frac{\omega_k D_k^2}{2\hbar}, \quad (5)$$

$$\lambda = \sum\nolimits_k \hbar\omega_k HR_k. \quad (6)$$

Here ω_k refers to the vibration frequency and D_k represents the normal coordinate displacement of mode k.

In addition, for identification and visualization of the weak interaction between two molecules in an aggregate state, a function (δ_g) is used to define the intermolecular interaction based on IGMH:

$$\delta G_{i,j}^{\text{pair}} = \int \delta g_{i,j}(r)\,\mathrm{d}r = \int [g_{i,j}^{\text{IGM}}(r) - g_{i,j}(r)]\,\mathrm{d}r, \quad i \in A,\ j \in B, \tag{7}$$

$$g_{i,j}(r) = |\nabla\rho_i(r) + \nabla\rho_j(r)|, \tag{8}$$

$$g_{i,j}^{\text{IGM}}(r) = |\nabla\rho_i(r)| + |\nabla\rho_j(r)|. \tag{9}$$

Here, A and B refer to the two fragments in which the interaction is to be investigated, and i and j represent the atoms in these two fragments, respectively. The atomic pair δg index is denoted as δG^{pair}. Accordingly, δG^{atom} (%) is defined to survey the percentage of an atom's contribution to the interaction between fragments:

$$\delta G_i^{\text{atom}} = \sum_{j\in B} \delta G_{i,j}^{\text{pair}}, \tag{10}$$

$$\delta G_i^{\text{atom}}(\%) = \frac{\delta G_i^{\text{atom}}}{\sum\limits_{j\in A} \delta G_j^{\text{atom}}} \times 100\%. \tag{11}$$

3. Results and discussion

3.1. Molecular structures

The molecular structures of (*R*)-lmNCz-SC$_b$, (*S*)-lmNCz-SC$_b$, (*R*)-lmNCz-SC$_p$, (*S*)-lmNCz-SC$_p$, and (*R*)-lmNBd are shown in Fig. 1. The molecular structures of complex and dimer are shown in Fig. S1. The geometry of the ground state (S_0), the first singlet excited state (S_1), the first triplet excited state (T_1), and the second triplet excited state (T_2) of (*R*)-lmNCz, (*S*)-lmNCz, and (*R*)-lmNBd molecules in the gas phase, acetonitrile solution, and solid phase are optimized. The calculated properties of the (*R*)-lmNCz molecule and the (*S*)-lmNCz molecule in the gas phase and in solution are very similar (see Table S1). The properties of (*R*)-lmNCz and (*S*)-lmNCz in the same crystal structure are also very similar, so (*R*)-lmNCz-SC$_b$ and (*R*)-lmNCz-SC$_p$ are selected for the next analysis. The relevant calculation results of (*S*)-lmNCz-SC$_b$ and (*S*)-lmNCz-SC$_p$ are shown in Figs. S2–S9 and Tables S1–S6.

The root of the mean squared displacement (RMSD) can be used to describe the configuration difference between the ground state and the excited state for (*R*)-lmNCz-SC$_b$, (*R*)-lmNCz-SC$_p$, and (*R*)-lmNBd, as shown in Fig. 2. Tables S7–S11 list some important geometric parameters and experimental data of (*R*)-lmNCz-SC$_b$, (*R*)-lmNCz-SC$_p$, (*R*)-lmNBd, complex, and dimer molecules in the S_0, S_1, T_1, and T_2 states. As shown in Fig. 2, the configuration changes between S_0 and S_1 show that distinct aggregation methods and distinct donors have different effects on the geometric changes during molecular excitation, where the RMSD values of (*R*)-lmNCz-SC$_b$, (*R*)-lmNCz-SC$_p$, and (*R*)-lmNBd are 0.082 Å, 0.077 Å, and 0.135 Å, respectively. In different aggregation modes, the bond lengths and bond angles of (*R*)-lmNCz-SC$_b$ and (*R*)-lmNCz-SC$_p$ are similar, but the dihedral angles of (*R*)-lmNCz-SC$_b$ and (*R*)-lmNCz-SC$_p$ are significantly different (as shown in Table S7 and S8). The change in dihedral angles of (*R*)-lmNCz-SC$_b$ (α_1 changes from $-6.0°$ to $4.4°$, α_2 changes from $2.1°$ to $-0.8°$) is significantly greater than that of (*R*)-lmNCz-SC$_p$ (α_1 changes from $-1.7°$ to $1.9°$, α_2 changes from $-3.9°$ to $-0.2°$) when they are changed from S_0 to S_1. Therefore, the larger dihedral angle change of (*R*)-lmNCz-SC$_b$ may increase the reorganization energy of a molecule. For (*R*)-lmNBd, the change in bond lengths and bond angles is also very small, mainly locating at the change of dihedral angles (α_1 changes from $16.3°$ to $8.8°$, α_2 changes from $-21.7°$ to $-8.9°$), which may make the non-radiative rate between S_0 and S_1 state of (*R*)-lmNBd very large. In contrast, the dihedral angles of (*R*)-lmNCz-SC$_b$ (α_1 changes from $4.4°$ to $1.1°$, α_2 changes from $-0.8°$ to $-4.5°$), (*R*)-lmNCz-SC$_p$ (α_1 changes from $-1.7°$ to $1.9°$, α_2 changes from $-0.8°$ to $-4.5°$), and (*R*)-lmNBd (α_1 changes from $8.8°$ to $7.1°$, α_2 changes from $-8.9°$ to $-12.5°$) have small differences, no more than $10°$, in the S_1 and T_1 state, which means their RMSD values are also smaller. The geometric difference between (*R*)-lmNCz-SC$_b$ and (*R*)-lmNCz-SC$_p$ in the S_1 and the T_2 state are small, and their RMSD values are also very small. This predicts a possible transition path from the high-energy excited state T_2 to the S_1 state. Dihedral angles of (*R*)-lmNBd, α_1 and α_2, change greatly in the S_1 and the T_2 state with α_1 changed by nearly $5.5°$ and α_2 changed by nearly $10.7°$, so the RMSD values of the S_1 and the T_2 state of (*R*)-lmNBd are large. At the same time, by analyzing the important geometric parameters of complex and dimer, it is found that the bond length and bond angle before and after optimization are little different, but the dihedral angle has changed. Therefore, we believe that the different aggregation modes and the changes of donor group will have a certain impact on the interaction between molecules, and then affect the molecular configuration.

Figure 3 shows the energy and distribution of frontier molecular orbitals. It is easy to find that the HOMO of (*R*)-lmNCz is mainly concentrated in the carbazole group, and the LUMO is mainly located in the phthalimide group. The HOMO–LUMO overlap of (*R*)-lmNCz-SC$_p$ is smaller than that of (*R*)-lmNCz-SC$_b$, which is related to the fact that the dihedral angle ($-61.94°$) between the phthalimide group and carbazole group of (*R*)-lmNCz-SC$_p$ is larger than the dihedral angle ($-46.99°$) between the phthalimide group and carbazole group of (*R*)-lmNCz-SC$_b$. This may be due to a stronger intermolecular interaction in the SC$_p$ crystal, which

makes the conformation of (*R*)-lmNCz-SC$_p$ molecule more distorted. The large dihedral angle makes the molecular conformation more distorted and the HOMO–LUMO overlap is small, which is conducive to reducing ΔE_{st}. The HOMO of (*R*)-lmNBd is mainly distributed in the benzoindole group, and the LUMO is mainly concentrated in the phthalimide group. Obviously, the dihedral angle between the phthalimide group and the benzoindole group in the (*R*)-lmNBd molecule is large (−79.77°), thus the HOMO–LUMO overlap is small and ΔE_{st} is also small. The HOMO–LUMO energy gap of (*R*)-lmNBd (2.393 eV) is obviously smaller than that of (*R*)-lmNCz-SC$_b$ (3.072 eV) and (*R*)-lmNCz-SC$_p$ (2.871 eV), so the emission of (*R*)-lmNBd has red shift. The frontier molecular orbital analysis of complex and dimer shows that the HOMO–LUMO distributions of the complex are analogous to those of (*R*)-lmNBd, and the HOMO–LUMO distributions of the dimer are similar to those of (*R*)-lmNCz-SC$_p$. It is found that the (*R*)-lmNBd will induce a smaller HOMO–LUMO energy gap.

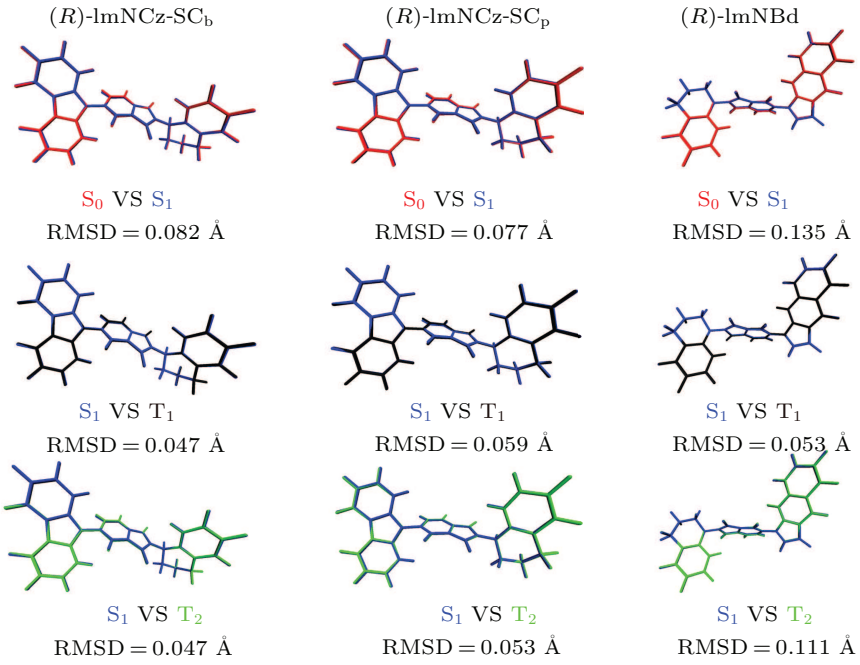


Fig. 2. RMSD of S_0 (red), S_1 (blue), T_1 (black), and T_2 (green) states for (*R*)-lmNCz-SC$_b$, (*R*)-lmNCz-SC$_p$, and (*R*)-lmNBd.

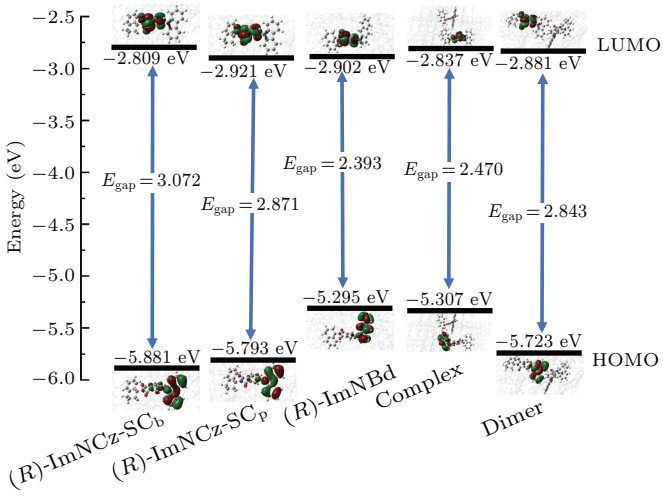


Fig. 3. Energies and electronic distributions of HOMO and LUMO for (*R*)-lmNCz-SC$_b$, (*R*)-lmNCz-SC$_p$, (*R*)-lmNBd, complex, and dimer in S_1 state in the solid phase.

3.2. Excited states

It is well known that the small energy gap between S_1 and T_n in TADF molecules and RTP molecules is an important parameter for rapid RISC and ISC processes. The adiabatic excitation energies of (*R*)-lmNCz in the two aggregation modes and (*R*)-lmNBd, complex, and dimer in the ONIOM model are shown in Table 2 and Fig. 4. The results reflect that the energy gaps between S_1 and S_0 of (*R*)-lmNCz-SC$_b$ and (*R*)-lmNCz-SC$_p$ (2.49 eV and 2.50 eV) are roughly equal, but the ΔE_{st} of (*R*)-lmNCz-SC$_p$ (0.13 eV) is smaller than that of (*R*)-lmNCz-SC$_b$ (0.21 eV) due to the higher triplet energy in SC$_p$ mode, which makes (*R*)-lmNCz-SC$_p$ more likely to exhibit TADF than (*R*)-lmNCz-SC$_b$. For (*R*)-lmNBd, both S_1 and T_1 become lower than (*R*)-lmNCz. The energy gap between them is also smaller. The energy gap between T_1 and S_0 of (*R*)-lmNBd (1.97 eV) is small, thus (*R*)-lmNBd is more likely to emit phosphorescence. Although the energy gap between S_1 and S_0 of the dimer (2.38 eV) is larger than that between S_1 and S_0 of the complex (2.25 eV), the ΔE_{st} of the dimer (0.13 eV) is smaller than that of the complex (0.16 eV), which makes the dimer more likely to display TADF than the complex. It is found that the energy gaps between T_1 and S_0 of the (*R*)-lmNBd, complex, and dimer increase in turn (1.97 eV, 2.09 eV, and 2.25 eV), indicating that the emission wavelength would shift blue. Introducing (*R*)-lmNBd would induce lower

excited states, and thus red shift emission.

Besides ΔE_{st}, the transition properties and SOC constants between the two electronic states are also important indicators to determine RISC and ISC processes. By analyzing the S_1, T_1, and T_2 states of (*R*)-lmNCz-SC_b, (*R*)-lmNCz-SC_p, (*R*)-lmNBd, complex, and dimer, the natural transition orbit (NTO) shown in Fig. 5 is obtained. All S_1 states and T_2 states have charge transfer (CT) characteristics, and T_1 states have hybridized local charge-transfer (HLCT) properties. The results show that there is only partial transfer between the acceptor group and the donor group of the T_1 state of (*R*)-lmNCz-SC_b and (*R*)-lmNCz-SC_p molecules, which would make the SOC between the S_1 state and the T_1 state larger. This helps to promote the intersystem crossover of excitons between the S_1 state and the T_1 state. The CT feature of the S_1 state is helpful to reduce the ΔE_{st}. It is found that different stacking patterns have little influence on the transition properties of the triplet excited states.

Table 2. Calculated emission wavelength for fluorescence (λ_{fl}) and photoluminescence (λ_{ph}), oscillator strength (f), transition dipole moment (μ), adiabatic singlet (E_{S1}) and triplet (E_{T1}) energies, adiabatic singlet–triplet energy gap (ΔE_{st}) of (*R*)-lmNCz-SC_b, (*R*)-lmNCz-SC_p, (*R*)-lmNBd, complex, and dimer in the solid phase.

	λ_{fl} (nm)	λ_{ph} (nm)	f	μ (Debye)	E_{S1} (eV)	E_{T1} (eV)	ΔE_{st} (eV)
(*R*)-lmNCz-SC_b	498	544	0.054	0.00239	2.49	2.28	0.21
(*R*)-lmNCz-SC_p	496	523	0.033	0.00106	2.50	2.37	0.13
(*R*)-lmNBd	607	630	0.060	0.00035	2.04	1.97	0.07
Complex	550	592	0.055	–	2.25	2.09	0.16
Dimer	521	551	0.037	–	2.38	2.25	0.13

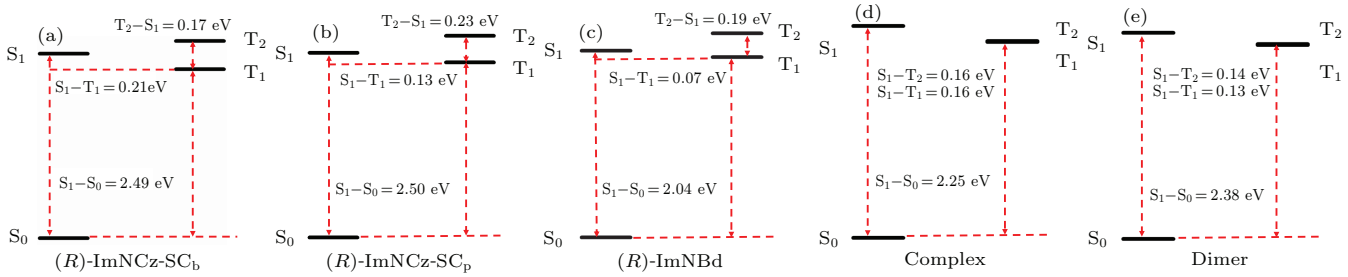


Fig. 4. Excitation energy for (*R*)-lmNCz-SC_b (a), (*R*)-lmNCz-SC_p (b), (*R*)-lmNBd (c), complex (d), and dimer (e) in the solid phase.

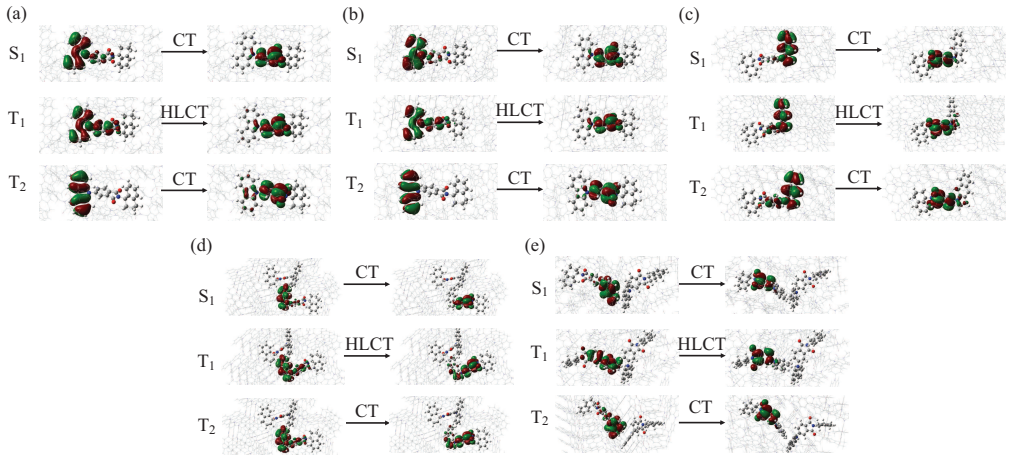


Fig. 5. Natural transition orbitals (NTOs) of the S_1, T_1, and T_2 states based on their optimized structures for (*R*)-lmNCz-SC_b (a), (*R*)-lmNCz-SC_p (b), (*R*)-lmNBd (c), complex (d), and dimer (e) in the solid phase.

3.3. Reorganization energy and intermolecular interactions

The non-radiative decay process between S_1 and S_0 and between T_1 and S_0 are closely related to structural transformation and electron–vibration coupling. For the sake of further exploring the non-radiative process under diverse aggregation modes, the relationships between the frequency and the reorganization energy of (*R*)-lmNCz-SC_b, (*R*)-lmNCz-SC_p, and (*R*)-lmNBd in S_1 and T_1 are shown in Figs. 6 and 7. The main dissipation channels of vibration relaxation can be divided into three parts: low-frequency (LF, < 500 cm^{-1}) mode, mid-frequency (MF, 500–1500 cm^{-1}) mode, and high-frequency (HF, > 1500 cm^{-1}) mode. The reorganization energy between S_1 and S_0 of (*R*)-lmNCz-SC_p is mainly contributed by MF and HF modes. Compared with (*R*)-lmNCz-SC_p, the reorganization energy between S_1 and S_0 of (*R*)-lmNCz-SC_b in LF mode is increased, especially the rotational contribution between the dihedral angle of donor and acceptor, such as

161.58 cm^{-1}. The increase in the dissipative pathway will increase the non-radiative decay process of molecules. In the (*R*)-lmNBd molecule, the reorganization energy between S_1 and S_0 is mainly contributed by LF and HF modes. In the LF mode, the bending vibration of the Bd group outward along the plane is the main contribution (115.91 cm^{-1}), while the contribution in the HF mode mainly comes from C=O stretching vibration (1902.15 cm^{-1}). The vibration modes of (*R*)-lmNBd between S_1 and S_0 and between T_1 and S_0 are similar, but the reorganization energy between T_1 and S_0 is significantly reduced, which is conducive to reducing the non-radiative dissipation from T_1 to S_0. Moreover, the C–H stretching vibration at about 3500 cm^{-1} also contributes to the reorganization energy for (*R*)-lmNBd.

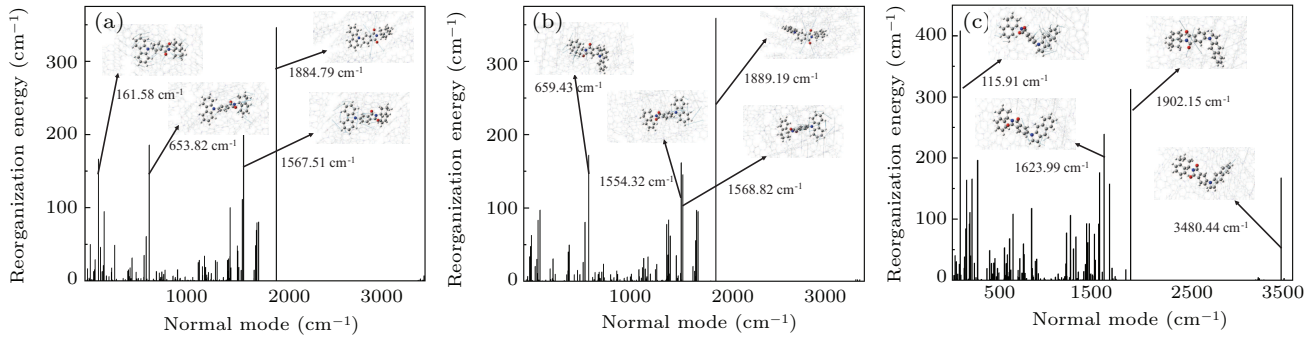


Fig. 6. Calculated reorganization energies versus the normal mode frequencies for (*R*)-lmNCz-SC_b (a), (*R*)-lmNCz-SC_p (b), and (*R*)-lmNBd (c) of the S_1 state in the solid phase. Representative vibration modes are shown as insets.

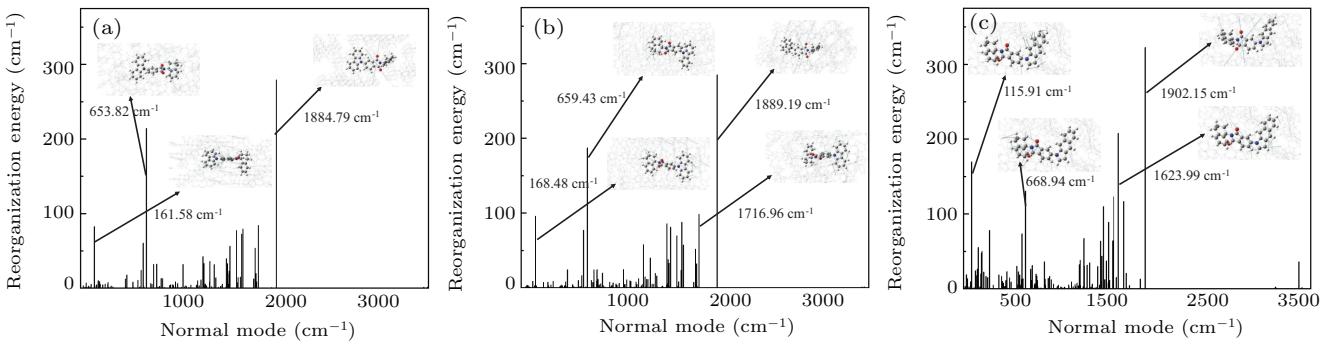


Fig. 7. Calculated reorganization energies versus the normal mode frequencies for (*R*)-lmNCz-SC_b (a), (*R*)-lmNCz-SC_p (b), and (*R*)-lmNBd (c) of the T_1 state in the solid phase. Representative vibration modes are shown as insets.

In order to study the influence of intermolecular stacking mode on intermolecular interactions, we used IGMH analysis to visually analyze weak interactions (as shown in Fig. 8). Although (*R*)-lmNCz-SC_b and (*R*)-lmNCz-SC_p are the same molecule, they do not stack in the same way. It can be seen that in the SC_b crystal, the intermolecular interactions of dimer-4 (−103.27 kJ/mol) and dimer-7 (−112.18 kJ/mol) are significantly stronger than those of other dimers, with obvious π–π stacking and some C–H–π interactions and C–H–O interactions. The large area in green between the adjacent phenyls of these two pairs of dimers shows that their intermolecular interactions are van der Waals interactions. In addition, it also shows representative characteristics of π–π stacking. The intermolecular interactions of dimer-6 (−3.64 kJ/mol) are the weakest. In other dimers, the intermolecular interactions are roughly the same. It is found that dimer-1 (−44.05 kJ/mol) and dimer-5 (−45.36 kJ/mol) are mainly carbazole–carbazole interactions, and dimer-2 (−30.76 kJ/mol) and dimer-3 (−31.32 kJ/mol) are mainly π–π stackings. In SC_p crystal, dimer-1 (−45.34 kJ/mol) has the strongest intermolecular interactions, including carbazole–carbazole interactions, C–H–π interactions, and C–H–O interactions. It can be seen that dimer-5 (−38.24 kJ/mol) and dimer-7 (−38.25 kJ/mol) are mainly carbazole–carbazole interactions, and dimer-1 (−36.53 kJ/mol) and dimer-3 (−6.53 kJ/mol) are mainly C–H–π interactions. There are weak carbazole–carbazole interactions between dimer-4 (−13.78 kJ/mol) and dimer-6 (−13.79 kJ/mol). We find that the strong intermolecular carbazole–carbazole interactions are conducive to the suppression of non-radiative channels. At the same time, we also analyzed the intermolecular interactions of the (*R*)-lmNBd molecule containing Bd impurity. The intermolecular interactions of dimer-1 (−47.99 kJ/mol) are the strongest, which are C–H–O interactions and C–H–π interactions. Dimer-2 (−31.02 kJ/mol) has strong C–H–Bd interactions, dimer-3 (−22.12 kJ/mol) and dimer-4 (−19.23 kJ/mol) are similar to dimer-2, but C–H–Bd interactions are weak. There are many Cz–Bd interactions in dimer-5 (−33.25 kJ/mol). dimer-6 (−8.98 kJ/mol) and dimer-7 (−8.12 kJ/mol) have weak Cz–Bd interactions. Obviously, the van der Waals interaction is

the most important intermolecular interaction of the three systems. The face-to-face stacking mode in the SC_b crystal makes the system form intermolecular interactions with a strong π–π stacking effect. The edge stacking mode of the SC_p crystal makes the system form obvious intermolecular carbazole–carbazole interactions. The impurity system we simulated has a special intermolecular Cz–Bd interaction.

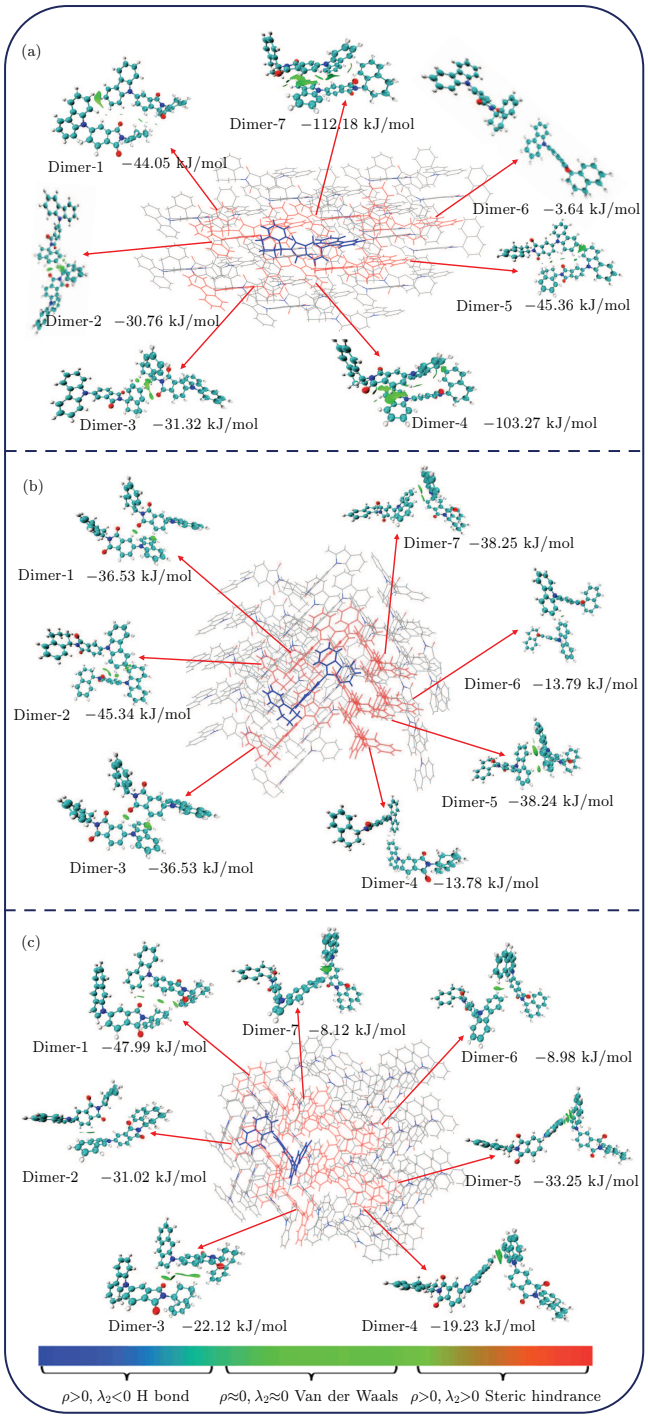


Fig. 8. Intermolecular interactions for selected dimers of (*R*)-lmNCz-SC_b (a), (*R*)-lmNCz-SC_p (b), and (*R*)-lmNBd (c) described by the IGMH method.

3.4. Excited state dynamics

In order to quantitatively analyze the photophysical properties of molecules, we calculated the SOC constant at room temperature, as shown in Table 3. For (*R*)-lmNCz-SC_p, the SOC constant between S_1 and T_1 (0.687 cm^{-1} and 0.492 cm^{-1}) is much larger than that SOC constant between S_1 and T_2 (0.069 cm^{-1} and 0.108 cm^{-1}), so the ISC processes and RISC processes occur more easily between S_1 and T_1. (*R*)-lmNCz-SC_b is similar to (*R*)-lmNCz-SC_p, and the SOC constant between S_1 and T_1 (0.588 cm^{-1} and 0.477 cm^{-1}) of (*R*)-lmNCz-SC_b is much larger than that between S_1 and T_2 (0.081 cm^{-1} and 0.090 cm^{-1}), so the ISC processes and RISC processes occur more easily between S_1 and T_1. It can be seen that the SOC constant of S_1–T_1 for (*R*)-lmNCz-SC_p based on the S_1 configuration (0.687 cm^{-1}) is greater than that of (*R*)-lmNCz-SC_b (0.588 cm^{-1}), which is prone to ISC and RISC processes. Therefore, it is reasonable to believe that the fluorescence peak measured in the (*R*)-lmNCz-SC_p crystal experiment partly comes from the transition of excitons from the T_1 state to the S_1 state, then radiates to the ground state for luminescence. For (*R*)-lmNCz-SC_p and (*R*)-lmNBd, the SOC constants between S_0 and T_1 calculated based on the S_0 configuration (2.782 cm^{-1} and 1.458 cm^{-1}) are also very large, which makes it possible to produce phosphorescence.

In addition, the calculated emission wavelength for fluorescence (λ_{fl}) and photoluminescence (λ_{ph}), oscillator strength (f), transition dipole moment (μ) of (*R*)-lmNCz-SC_b, (*R*)-lmNCz-SC_p, (*R*)-lmNBd, complex, and dimer in the solid phase are shown in Table 2. It can be seen that the 430–520 nm fluorescence peak of the crystal in the experiment may be the joint action of (*R*)-lmNCz-SC_p (496 nm) and dimer (521 nm). In the experiment, the three phosphorescence peaks of the crystal come from various sources. The phosphorescence emission peak at 550 nm may be the joint action of (*R*)-lmNCz-SC_p (523 nm) and dimer (551 nm). The phosphorescence emission peak at 600 nm may be due to complex (592 nm) effect. The phosphorescence emission peak at 650 nm may be caused by (*R*)-lmNBd (630 nm). The phosphorescence peak at 550 nm has more sources than the ones at 600 nm and 650 nm, so the peak at 550 nm is more obvious. At the same time, we calculated K_r, K_{nr}, K_{ISC}, and K_{RISC}, as shown in Tables 4 and 5. The K_r^1 of (*R*)-lmNCz-SC_p (6.94×10^7 s^{-1}) is obviously larger than that of (*R*)-lmNCz-SC_b (1.12×10^7 s^{-1}), so it is easier for (*R*)-lmNCz-SC_p to fluoresce. At the same time, K_{ISC}^1 and K_{RISC}^1 of (*R*)-lmNCz-SC_p (1.83×10^8 s^{-1}, 1.93×10^6 s^{-1}) are also very large, which is conducive to enhancing fluorescence emission. K_r^2 and K_{nr}^2 of (*R*)-lmNCz-SC_p and (*R*)-lmNBd are relatively small (2.6×10^0 s^{-1}, 1.04×10^3 s^{-1} s^{-1}, 1.9×10^{-1}, 4.95×10^5 s^{-1}), but the intersystem transition process from the S_1 state to the T_1 state of (*R*)-lmNCz-SC_p and (*R*)-lmNBd (1.83×10^8 s^{-1} and 2.81×10^8 s^{-1}, respectively) are fast, which makes excitons accumulate in the T_1 state and promotes the T_1–S_0 radiative process.

Table 3. Calculated SOC constants between S_1 and T_1, between S_0 and T_1, and between S_1 and T_2 for (*R*)-lmNCz-SC_b, (*R*)-lmNCz-SC_p, and (*R*)-lmNBd in the solid phase based on optimized S_1, T_1, and T_2 structures.

	$\langle S_1\|\hat{H}_{so}\|T_1\rangle$	$\langle T_1\|\hat{H}_{so}\|S_1\rangle$	$\langle S_0\|\hat{H}_{so}\|T_1\rangle$	$\langle S_1\|\hat{H}_{so}\|T_2\rangle$	$\langle T_2\|\hat{H}_{so}\|S_1\rangle$
(*R*)-lmNCz-SC_b	0.588	0.477	2.232	0.081	0.090
(*R*)-lmNCz-SC_p	0.687	0.492	2.782	0.069	0.108
(*R*)-lmNBd	0.479	0.322	1.458	0.418	0.367

Table 4. Rate constants of radiative and non-radiative between S_0 and S_1 (K_r^1, K_{nr}^1) and between S_0 and T_1 (K_r^2, K_{nr}^2) for (*R*)-lmNCz-SC_b, (*R*)-lmNCz-SC_p, and (*R*)-lmNBd in the solid phase.

	K_r^1 (s^{-1})	K_{nr}^1 (s^{-1})	K_r^2 (s^{-1})	K_{nr}^2 (s^{-1})
(*R*)-lmNCz-SC_b	1.12×10^7	8.91×10^7	1.42×10^1	1.43×10^3
(*R*)-lmNCz-SC_p	6.94×10^7	5.69×10^7	2.60×10^{00}	1.04×10^3
(*R*)-lmNBd	1.74×10^7	3.55×10^9	1.9×10^{-1}	4.95×10^5

Table 5. Effective intersystem crossing (ISC) rates and reverse intersystem crossing (RISC) rates between S_1 and T_1 (K_{ISC}^1, K_{RISC}^1) and between S_1 and T_2 (K_{ISC}^2, K_{RISC}^2) for (*R*)-lmNCz-SC_b, (*R*)-lmNCz-SC_p, and (*R*)-lmNBd in the solid phase.

	K_{ISC}^1 (s^{-1})	K_{RISC}^1 (s^{-1})	K_{ISC}^2 (s^{-1})	K_{RISC}^2 (s^{-1})
(*R*)-lmNCz-SC_b	6.74×10^7	2.52×10^4	1.24×10^1	1.62×10^6
(*R*)-lmNCz-SC_p	1.83×10^8	1.93×10^6	1.78×10^{-1}	1.05×10^6
(*R*)-lmNBd	2.81×10^8	3.17×10^7	–	–

4. Conclusions

In conclusion, the photophysical properties of (*R*)-lmNCz in two different aggregation modes are systematically studied based on QM/MM calculations, and the sources of multiple emission peaks detected in experiments are explained. The results show that the aggregation modes can lead to different energy diagrams of electronic states and emission wavelengths. The excited states of (*R*)-lmNCz-SC_b and (*R*)-lmNCz-SC_p have similar transition properties, but (*R*)-lmNCz-SC_b has more vibrational modes than (*R*)-lmNCz-SC_p, which increases the reorganization energy of (*R*)-lmNCz-SC_b and increases non-radiative process. For (*R*)-lmNCz-SC_p, larger SOC and smaller ΔE_{st} favor the generation of TADF. In addition, it is verified that the generation of a phosphorescence peak in the SC_p crystal may be related to a small amount of (*R*)-lmNBd impurity in the crystal. The phosphorescence peak at 550 nm has one more source than that at 600 nm and 650 nm, so the phosphorescence peak of 550 nm is a little stronger. Our calculated results are in good agreement with the experimental results. In addition, the influence of the impurity on emission spectra is also confirmed theoretically, which adds to the understanding of the luminescent properties of TADF molecules in aggregation.

Data availability statement

The data that support the findings of this study are openly available in Science Data Bank at https://doi.org/10.57760/sciencedb.j00113.00093.

Acknowledgements

Project supported by the National Natural Science Foundation of China (Grant Nos. 11974216, 11874242, 21933002 and 11904210) and Shandong Provincial Natural Science Foundation, China (Grant No. ZR2019MA056). The authors acknowledge the support of the Taishan Scholar Project of Shandong Province and the project funded by China Postdoctoral Science Foundation (Grant No. 2018M642689).

References

[1] Tang C W and Vanslyke S A 1987 *Appl. Phys. Lett.* **51** 913
[2] Reineke S, Lindner F, Schwartz G, Seidler N, Walzer K, Lussem B and Leo K 2009 *Nature* **459** 234
[3] Yoshida K, Masui K, Nakanotani H and Adachi C 2016 *Org. Electron.* **31** 191
[4] Guo D, Xu Z, Yang D, Ma D, Tang B and Vadim A 2020 *Nanoscale* **12** 2648
[5] Pope M 1968 *Mol. Cryst.* **4** 183
[6] Zhang H, Zhang B, Zhang Y, Xu Z, Wu H, Yin P A, Wang Z, Zhao Z, Ma D and Tang B Z 2020 *Adv. Funct. Mater.* **30** 2002323
[7] Li F Y, Li M Z, Fan J Z, Song Y Z, Wang C K and Lin L L 2020 *J. Phys. Chem. A* **124** 7526
[8] Wang Y, Peng Q, Ou Q, Lin S Y and Shuai Z G 2020 *J. Mater. Chem. A* **8** 18721
[9] Baldo M A, O'Brien D F, You Y, Shoustikov A, Sibley S, Thompson M E and Forrest S R 1998 *Nature* **395** 151
[10] Jiang G Y, Li F Y, Fan J Z, Song Y Z, Wang C K and Lin L L 2020 *J. Mater. Chem. C* **8** 98
[11] Ni F, Li N Q, Zhan L S and Yang C L 2020 *Adv. Optical Mater.* **8** 1902187
[12] Zhao M L, Zhang H H, Gu C and Ma Y G 2020 *J. Mater. Chem. C* **8** 5310
[13] Liu S S, Lu J J, Lu Q, Fan J Z, Lin L L, Wang C K and Song Y Z 2019 *Front. Chem.* **7** 932
[14] Ma H L, Lv A Q, Fu L S, Wang S, An Z F, Shi H F and Huang W 2019 *Ann. Phys.* **7** 531
[15] Sarma M and Wong K T 2018 *ACS Appl. Mater. Inter.* **10** 19279
[16] Tao Y, Yuan K, Chen T, Xu P, Li H H, Chen R F, Zheng C, Zhang L and Huang W 2014 *Adv. Mater.* **26** 7931
[17] Hsieh C M, Wu T L, Jayakumar J, Wang Y C, Ko C L, Hung W Y, Lin T C, Wu H H, Lin K H, Lin C H, Hsieh S C and Cheng C H 2020 *ACS Appl. Mater. Inter.* **12** 23199
[18] Zhong D K, Yu Y, Song D D, Yang X L, Zhang Y D, Chen X, Zhou G J and Wu Z X 2019 *ACS Appl. Mater. Inter.* **11** 27112
[19] Olivier Y, Sancho-Garcia J C, Muccioli L, D'Avino G and Beljonne D 2018 *J. Phys. Chem. Lett.* **9** 6149
[20] Ye J T, Wang L, Wang H Q, Xie H M and Qiu Y Q 2019 *Org. Electron.* **70** 193
[21] Tsai C C, Huang W C, Chih H Y, Hsh Y C, Liao C W, Lin C H, Kang Y X, Chang C H, Chang Y J and Lu C W 2018 *Org. Electron.* **63** 166
[22] dos Santos P L, Etherington M K and Monkman A P 2018 *J. Mater. Chem. C* **6** 4842
[23] Liu J J, Hu T P, Li Z Y, Wei X F, Hu X X, Gao H L, Liu G H, Yi Y P, Yamada-Takamura Y, Lee C S, Wang P and Wang Y 2019 *J. Phys. Chem. Lett.* **10** 1888
[24] Sarkar S K, Pegu M, Behera S K, Narra S K and Thilagar P 2019 *Chem. Asian J.* **14** 4588
[25] Zheng K L, Ni F, Chen Z X, Zhong C and Yang C L 2020 *Angew. Chem. Int. Ed.* **59** 9972

[26] Yang W, Yang Y Y, Cao X S, Liu Y, Chen Z X, Huang Z Y, Gong S L and Yang C L 2021 *Chem. Eng. J.* **415** 128909
[27] Zhu J L, Liao Q, Huang H, Fu L Y, Liu M H, Gu C L and Fu H B 2022 *Cell Rep. Phys. Sci.* **3** 1
[28] Li J A, Song Z C, Chen Y T, Xu C, Li S F, Peng Q E, Shi G, Liu C, Luo S L, Sun F Q, Zhao Z J, Chi Z G, Zhang Y and Xu B J 2021 *Chem. Eng. J.* **418** 129167
[29] Li M Z, Li F Y, Zhang Q, Zhang K, Song Y Z, Fan J Z, Wang C K and Lin L L 2021 *Chin. Phys. B* **30** 123302
[30] Zhang K, Zhang X, Fan J Z, Song Y Z, Fan J Z, Wang C K and Lin L L 2022 *J. Phys. Chem. Lett.* **13** 4711
[31] Chen C J, Chi Z G, Chong K C, Batsanov A S, Yang Z, Mao Z, Yang Z Y and Liu B 2021 *Nat. Mater.* **20** 175
[32] Fan J Z, Lin L L and Wang C K 2016 *Chem. Phys. Lett.* **652** 16
[33] Fan D, Yi Y P, Li Z D, Liu W J, Peng Q and Shuai Z G 2015 *J. Phys. Chem. A* **119** 5233
[34] Chung L W, Sameera W M C, Ramozzi R, Page A, Hatanaka M P, Petrova G V, Harris T, Li X, Ke Z F, Liu H B, Ding L N and Morokuma K 2015 *Chem. Rev.* **115** 5678
[35] Ruiz-Barragan S, Morokuma K and Blancafort L 2015 *J. Chem. Theory Comput.* **11** 1585
[36] Fan J Z, Zhang Y C, Zhou Y, Lin L and Wang C K 2018 *J. Phys. Chem. C* **122** 2358
[37] Fan J Z, Zhang Y C, Zhang K, Liu J, Jiang G Y, Lin L L and Wang C K 2019 *Org. Electron.* **71** 113
[38] Runge E and Gross E K U 1984 *Phys. Rev. Lett.* **52** 997
[39] Zhang K, Zhang Q, Li M Z, Song Y Z, Fan J Z, Wang C K and Lin L L 2022 *J. Phys. Chem. C* **126** 2437
[40] Zhang K, Wang X F, Zhang Q, Wu Z M, Li X F, Mu Q F, Fan J Z, Wang C K and Lin L L 2022 *Spectrochim. Acta Part A: Mol. Biomol. Spectrosc.* **278** 121328
[41] Lu T and Chen Q 2022 *J. Comput. Chem.* **43** 539
[42] Miehlich B, Savin A, Stoll H and Preuss H 1989 *Chem. Phys. Lett.* **157** 200
[43] Adamo C and Barone V 1999 *J. Chem. Phys.* **110** 6158
[44] Boese A D and Martin J M 2004 *J. Chem. Phys.* **121** 3405
[45] Zhao Y and Truhlar D G 2007 *Theor. Chem. Acc.* **120** 215
[46] Chai J D and Head-Gordon M 2008 *Phys. Chem. Chem. Phys.* **10** 6615
[47] Frisch M J, Trucks G W, Schlegel H B, *et al. Gaussian 16*, Rev. A. 03, Inc., Wallingford, C T, 2016
[48] Gao Y J, Chen W K, Zhang T T, Fang W H and Cui G 2018 *J. Phys. Chem. C* **122** 27608
[49] Fan J Z, Zhang Y C, Zhang K, Lin L L and Wang C K 2019 *J. Lumin.* **209** 372
[50] Dalton, a molecular electronic structure program, release v2020.1. DOI: http://daltonprogram.org
[51] Niu Y L, Li W Q, Peng Q, Geng H, Yi Y P, Wang L J, Nan G J, Wang D and Shuai Z G 2018 *Mol. Phys.* **116** 1078
[52] Lv A Q, Yu Z, Mao Y F, Zheng X Y, Shi W, Shi H F, Yao W, Ma H L and An Z F 2021 *Dyes Pigments* **193** 109520
[53] Shuai Z G, Wang D, Peng Q and Geng H 2014 *Acc. Chem. Res.* **47** 3301
[54] Peng Q, Shi Q H, Niu Y L, Yi Y P, Sun S R, Li W Q and Shuai Z G 2016 *J. Mater. Chem. C* **4** 6829